ROYAL SOCIETY
OF CHEMISTRY

PCCP

Mixed Iron-Manganese Based Pyrophosphate Cathode, Na2Fe0.5Mn0.5P2O7, for Rechargeable Sodium Ion Batteries

SCHOLARONE™
Manuscripts

PCCP

ARTICLE

Mixed Iron-Manganese Based Pyrophosphate Cathode, $Na_2Fe_{0.5}Mn_{0.5}P_2O_7$, for Rechargeable Sodium Ion Batteries

Rana A. Shakoor,*[a,||] Chan Sun Park,[b,||] Arsalan A. Raja[c, §], Jaeho Shin,[b] Ramazan Kahraman*[c]

The development of secondary batteries based on abundant and cheap elements is vital. Among various alternatives to conventional lithium-ion batteries, sodium-ion batteries (SIBs) are promising due to the abundant resources and low cost of sodium. While there are many challenges associated with SIB system, cathode is an important factor in determining the electrochemical performance of this battery system. Accordingly, ongoing research in the field of SIBs is inclined towards the development of safe, cost effective cathode materials having improved performance. In particular, pyrophosphate cathodes have recently demonstrated decent electrochemical performance and thermal stability. Herein, we report the synthesis, electrochemical properties, and thermal behavior of a novel $Na_2Fe_{0.5}Mn_{0.5}P_2O_7$ cathode for SIBs. The material was synthesized through a solid state process. The structural analysis reveals that the mixed substitution of manganese and iron has resulted in a triclinic crystal structure (*P-1* space group). Galvanostatic charge/discharge measurements indicates that $Na_2Fe_{0.5}Mn_{0.5}P_2O_7$ is electrochemically active with a reversible capacity of ~80 mAh/g at C/20 rate with an average redox potential of 3.2 V. (vs. Na/Na$^+$). It is noticed that 84% of initial capacity is preserved over 90 cycles showing promising cyclability. It is also noticed that the rate capability of $Na_2Fe_{0.5}Mn_{0.5}P_2O_7$ is better than $Na_2MnP_2O_7$. Ex situ and and CV analyses indicate that $Na_2Fe_{0.5}Mn_{0.5}P_2O_7$ undergoes a single phase reaction rather than a biphasic reaction due to different Na coordination environment and different Na sites occupancy when compared to other pyrophosphate mterials ($Na_2FeP_2O_7$ and $Na_2MnP_2O_7$).Thermogravimetric analysis (25-550°C) confirms good thermal stability of $Na_2Fe_{0.5}Mn_{0.5}P_2O_7$ with only 2% weight loss. Owing to promising electrochemical properties and decent thermal stability, $Na_2Fe_{0.5}Mn_{0.5}P_2O_7$, can be an attractive cathode for SIBs.

Introduction

Lithium-ion batteries (LIBs) have succeeded to find a wide range of applications, from portable electronics to electric vehicles[1]. The recent trend of extending battery systems, especially towards electric vehicles and energy storage systems (ESS), has given rise to a serious concern of the cost and abundance of Li resources. Hence, recently sodium-ion batteries (SIBs) have emerged as an attractive replacements for LIBs [2, 3] based on cheap and easily accessible resources of sodium [3, 4]. In addition, much of the knowledge on the electrolyte and electrode phenomena accumulated during research of LIBs can be utilized to that of SIBs [5]. However, lower energy density and inferior kinetics, originating from the large size of Na ion, are serious challenges that must be overcome. Accordingly, a variety of crystal structures for cathode materials have been explored to address these

drawbacks [6-8]. Among them, pyrophosphate materials are quite attractive due to their open and stable crystal structure enabling easier movement of sodium ions during the battery operation. There are few reported pyrophosphate cathode materials for sodium-ion batteries [8-12]. Among them, $Na_2FeP_2O_7$ has shown promising reversible capacity (80 mAh/g) and rate capability [8]. $Na_2MnP_2O_7$ has also exhibited a reversible capacity of ~90 mAh/g at 3.8 V (vs. Na/Na$^+$) with 96% capacity retention after 30 cycles at scan rate of C/20 [11]. However, $Na_2MnP_2O_7$ is suffering from limited rate capability due to the intrinsic lower electronic conductivity of Mn. In addition, it is also reported that Mn-based polyanionic materials demonstrate inferior thermal stability than that of Fe-based polyanionic materials [13, 14]. Improving properties of materials by the addition of transition metals is quite attractive and many reports can be found in the literature [15, 16]. Thus, we designed a mixed transition metal (TM) pyrophosphate material to improve the rate performance and thermal stability of Mn-based pyrophosphate materials. The $Na_2Fe_{0.5}Mn_{0.5}P_2O_7$ was synthesized via solid state reaction. This work describes the structural, thermal and electrochemical performance of novel $Na_2Fe_{0.5}Mn_{0.5}P_2O_7$ cathode materials which has not been reported earlier.

[a.] Center for Advanced Materials (CAM), Qatar University, Doha 2713, Qatar. Tel.: +974 4403 6867 Email: shakoor@qu.edu.qa

[b.] Graduate School of EEWS, Korea Advanced Institute of Science and Technology, 291 Daehak-ro, Daejeon 305-701, Republic of Korea

[c.] Department of Chemical Engineering, College of Engineering, Qatar University, Doha 2713, Qatar. Tel.: +974 4403 4124 Email: ramazank@qu.edu.qa

* corresponding authors, || equal contribution § prepared manuscript
See DOI: 10.1039/x0xx00000x

Results and discussion
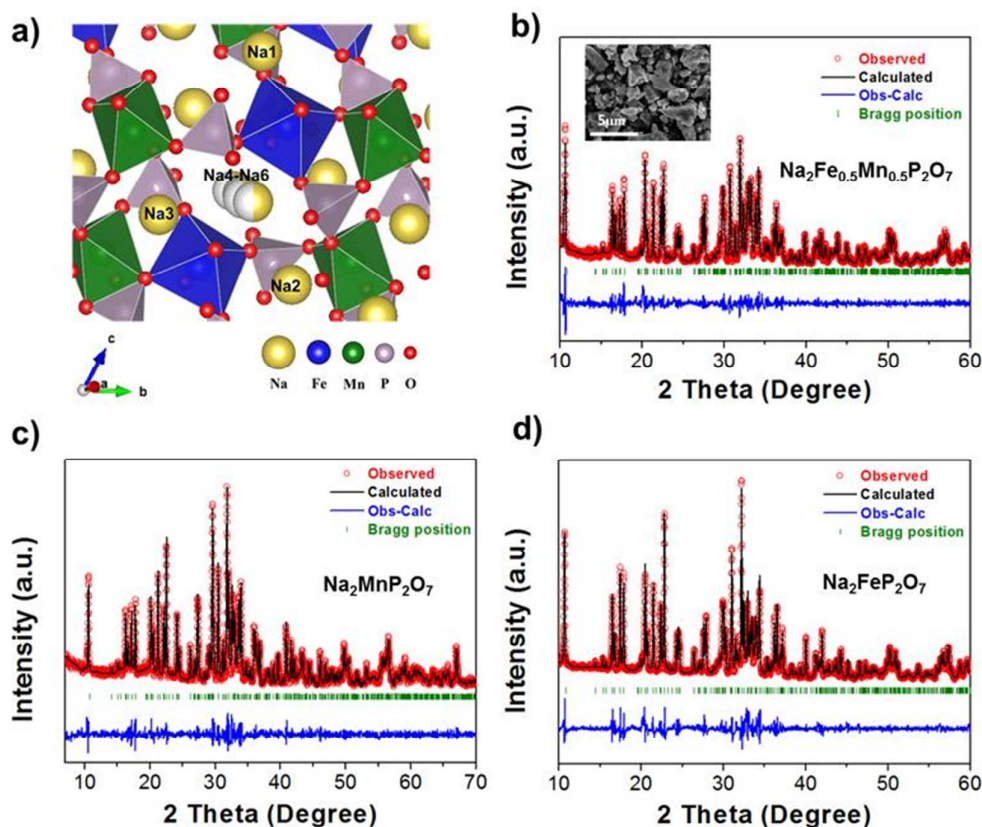
Fig. 1 a) A triclinic crystal structure (space group: P-1) b) The XRD profile and whole pattern indexing of $Na_2Fe_{0.5}Mn_{0.5}P_2O_7$ (R_p = 2.88, R_{wp} = 4.01 χ^2 = 1.77) Inset: SEM image showing the size of 3~5 μ m as-synthesized particles c) The XRD profile and whole pattern indexing of $Na_2MnP_2O_7$ (R_p = 9.38, R_{wp} = 13.07 χ^2 = 2.63) d) The XRD profile and whole pattern indexing of $Na_2FeP_2O_7$ (R_p = 4.06, R_{wp} = 6.00 χ^2 = 1.72)

Crystal Structure

Sodium pyrophosphate materials adopt different crystal structures depending on the types of transition metals used and synthetic conditions: M=Ni, (triclinic), Zn (tetragonal), Co (both orthorhombic and triclinic) [17-19]. Among them, triclinic structures have open frameworks which facilitate Na-ion diffusion during battery operation. The $Na_2MP_2O_7$ (M=Fe, Mn) family is indexed to triclinic framework which is isostructural with triclinic $Na_2CoP_2O_7$ [17] and $Na_{3.64}Ni_{2.18}(P_2O_7)_2$ [20]. The triclinic crystal structure can be described by a framework comprising corner-shared M_2O_{11} [MO_6-MO_6] dimers, sharing one oxygen atom and each MO_6 unit being separated by PO_4 or P_2O_7 groups (Figure 1a). In the environment of MO_6 sites, one MO_6 octahedron (blue) is connected to P_2O_7 by corner-sharing and the other distorted MO_6 (green) octahedron is linked by both corner-sharing and edge-sharing. The Na ions occupy six crystallographic sites (Na1-Na6).

The X-ray diffraction (XRD) data for as-synthesized $Na_2Fe_{1-x}Mn_xP_2O_7$ (x=0,0.5,1) was indexed to a triclinic structure

and the rietveld refined XRD spectra is presented in Figure 1 (b, c and d). The lattice parameters of $Na_2FeP_2O_7$ and $Na_2MnP_2O_7$ are also tabulated in Table 1 for a clear comparison. As shown in Figure 2, the values of the lattice parameters of $Na_2Fe_{0.5}Mn_{0.5}P_2O_7$ lie in between the lattice constants of $Na_2FeP_2O_7$ and $Na_2MnP_2O_7$, indicating solid solution formation based on Vegard's law.

In the family of pyrophosphates, It has been reported that $Na_2FeP_2O_7$ and $Na_2MnP_2O_7$ have difference in occupancy of Na cations [21, 22].

All Na sites are fully occupied in $Na_2MnP_2O_7$ while $Na_2FeP_2O_7$ contains either full or partially occupied Na sites. Therefore, we anticipate that the Na occupancy of partially occupied Na sites may have changed by the mixing of Fe and Mn to form a solid solution of $Na_2Fe_{0.5}Mn_{0.5}P_2O_7$. As shown in Fig. 1a, there are partially occupied Na4-Na6 sites and fully occupied Na1-Na3 sties in the crystal structure of $Na_2Fe_{0.5}Mn_{0.5}P_2O_7$. To clarify the change in the occupancy of Na sites, we performed galvanostatic measurements for first and second cycles (Figure 3).
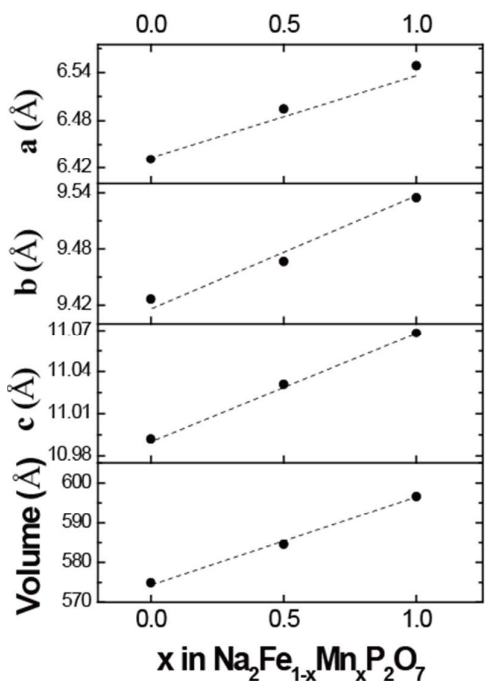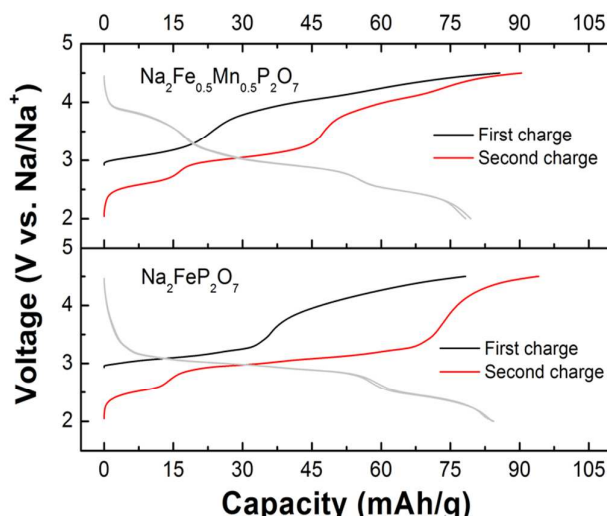
Table 1: The lattice parameters of $Na_2Fe_{1-x}Mn_xP_2O_7$ (x=0, 0.5, 1)

Materials	a (Å)	b (Å)	c (Å)	α (°)	β (°)	γ (°)	V (Å^3)
$Na_2FeP_2O_7$	6.4310	9.4264	10.992	64.687	79.707	72.989	574.9
$Na_2Fe_{0.5}Mn_{0.5}P_2O_7$	6.4945	9.4666	11.031	64.941	79.826	72.802	584.6
$Na_2MnP_2O_7$	6.5484	9.5347	11.068	64.444	79.830	73.155	596.6

In the first and second cycles of $Na_2FeP_2O_7$, the charge capacities of the first and second cycles shows a difference of approximately 15 mAh/g, which indicates that 0.16 Na ion are unoccupied. On the other hand, the first and second charge capacity difference of $Na_2Fe_{0.5}Mn_{0.5}P_2O_7$ is only 5 mAh/g (0.07 Na ion per formula unit), confirming increased Na occupancy in $Na_2Fe_{0.5}Mn_{0.5}P_2O_7$ as compared to the case of $Na_2FeP_2O_7$. Thus, from the charge-discharge profile, the changed occupancy of Na ions can be clearly observed.

Electrochemical Measurements

The galvanostatic initial charge/discharge analysis of $Na_2Fe_{0.5}Mn_{0.5}P_2O_7$ at a scan rate of C/20 is presented in Figure 4a. It can be noticed that $Na_2Fe_{0.5}Mn_{0.5}P_2O_7$ demonstrates a charge capacity of ~90 mAh/g and a discharge capacity of ~80mAh/g, respectively, in a potential range of 2 ~ 4.5 V (vs. Na/Na$^+$). The 2.5 V and 3.1V plateaus represent the activation of the $Fe^{+2/+3}$ redox couple while the plateau at 3.8 V confirms the activity of the Mn^{2+}/Mn^{3+} redox couple.

Fig. 3 First and second galvanostatic profile of $Na_2FeP_2O_7$ and $Na_2Fe_{0.5}Mn_{0.5}P_2O_7$ at C/20

Interestingly, unlike $Li_2Fe_{0.5}Mn_{0.5}P_2O_7$ [23, 24] the $Mn^{2+/3+}$ redox couple is active in $Na_2Fe_{0.5}Mn_{0.5}P_2O_7$. The monoclinic $Li_2MnP_2O_7$ has edge-shared Mn sites with multiple bonds which experience bond breakage during charging and discharging due to Jahn-teller distortion. On the other hand, triclinic $Na_2MnP_2O_7$ has corner-shared Mn sites that enables it to accommodate Jahn-teller distortion [11]. In terms of cyclic performance, 84% of the initial capacity (80 mAh/g) is preserved as reversible capacity in 90 cycles, indicating the stability of the framework upon Na insertion/de-insertion. In addition, the coulombic efficiency reaches a satisfactory value of 95% even after 90 cycles (Figure 4b).

The rate capability of $Na_2Fe_{0.5}Mn_{0.5}P_2O_7$ is presented in Figure 4c. It can be seen that when the C-rate is increased ten-fold from 0.05C to 0.5C, the discharge capacity of $Na_2Fe_{0.5}Mn_{0.5}P_2O_7$ is dropped from 80mAh/g to 56mAh/g. Whereas $Na_2MnP_2O_7$ experiences relatively a bigger drop in discharge capacity under the same conditions. The discharge capacity drops from 60 mAh/g to 47mAh/g (Figure 4d). This comparison reveals that the rate capability of $Na_2Fe_{0.5}Mn_{0.5}P_2O_7$ is better than $Na_2MnP_2O_7$. The rate capability of $Na_2Fe_{0.5}Mn_{0.5}P_2O_7$ is dropped with mixing of Mn when compared with $Na_2FeP_2O_7$ [8] which is in turn associated to the inferior kinetics of Mn. At the same time, it is pertinent to note that the discharge capacity of $Na_2Fe_{0.5}Mn_{0.5}P_2O_7$ is higher than $Na_2MnP_2O_7$ at all

Fig. 2 The linear variation of lattice parameters in the $Na_2Fe_{1-x}Mn_xP_2O_7$ (x=0, 0.5, 1)

PCCP

ARTICLE
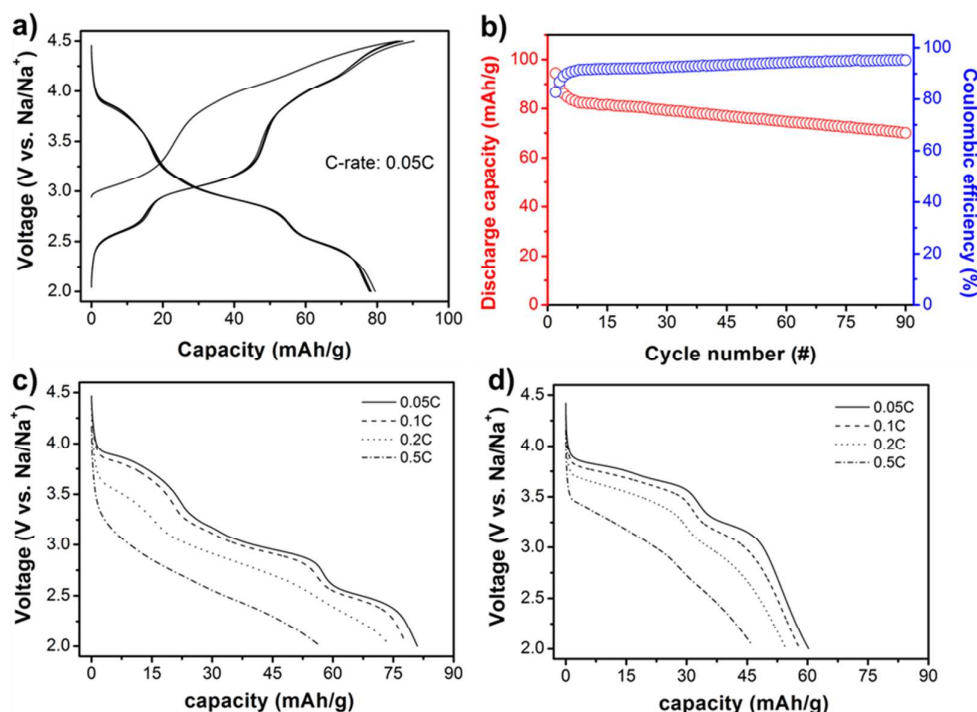
Fig. 4 (a) Voltage profile of $Na_2Fe_{0.5}Mn_{0.5}P_2O_7$ (b) Cycle performance of $Na_2Fe_{0.5}Mn_{0.5}P_2O_7$ (c) Rate capability test of $Na_2Fe_{0.5}Mn_{0.5}P_2O_7$ (d) Rate capability test of $Na_2MnP_2O_7$

C-scan rates (from 0.05C to 0.5C). In particular, the $Na_2MnP_2O_7$ shows 45 mAh/g at 0.5C which is lower than $Na_2Fe_{0.5}Mn_{0.5}P_2O_7$ (60 mAh/g at 0.5C). It can be further noticed, although the rate capacity retention of $Na_2Fe_{0.5}Mn_{0.5}P_2O_7$ is dropped as compared to $Na_2FeP_2O_7$, the amount of Na ion's transfer of $Na_2Fe_{0.5}Mn_{0.5}P_2O_7$ is higher than $Na_2MnP_2O_7$ at high C-rate. (0.5 vs. 0.7 Na ion per formula weight). Mn-based cathodes have inherently lower conductivity than Fe-based cathodes, causing relatively limited rate capability [25]. Thus, incorporation of more conductive metals such as Fe has improved the rate capability of $Na_2MnP_2O_7$.

In layered materials for SIB cathodes such as P2-Na_xCO_2, P2-$Na_{2/3}Co_{2/3}Mn_{1/3}O_2$ phase transitions are known to occur depending on the amount of Na ions, which in turn affect the coordination of Na sites [26-28]. To investigate the structural rearrangement by Na occupancy change in $Na_2Fe_{0.5}Mn_{0.5}P_2O_7$, we performed cyclic voltammetry (CV) measurements at a scan rate of 0.05 mV/s (Figure 5a). In the CV data, broad redox peaks can be observed at 2.5 V, 3.1 V ($Fe^{2+/3+}$) and 3.8 V ($Mn^{2+/3+}$), indicating a single-phase reaction. To further clarify the phase reaction, cyclic voltammetry (CV) measurements at a slower scan rate of 0.01mV/s were conducted (Figure 5a).
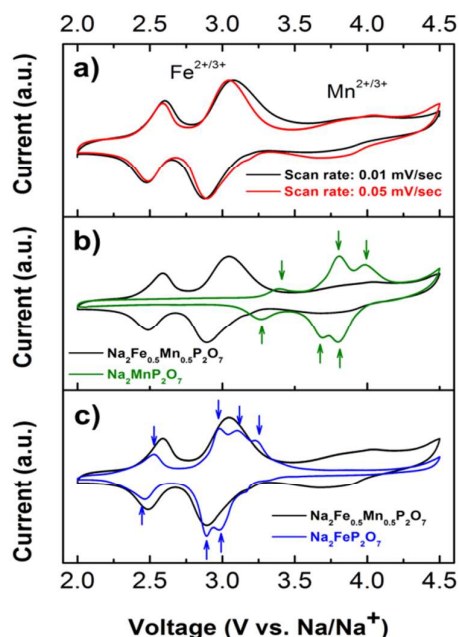
.**Fig. 5** Cyclic voltammetry (CV) data for $Na_2Fe_{0.5}Mn_{0.5}P_2O_7$, $Na_2MnP_2O_7$ and $Na_2FeP_2O_7$ at scan rate of 0.05 mV/s.

PCCP

ARTICLE

It has been reported that region at 2.5V defines a single-phase reaction while the region at 3V region represents a two-phase transition [8, 12]. In particular, the three peaks around 3V transition depend on the scan rate conditions. At a slower scan rate, peak separation becomes sharper indicating a two-phase reaction. The CV data of $Na_2Fe_{0.5}Mn_{0.5}P_2O_7$ shows broad redox peaks in the entire voltage range even at a slower rate suggesting existence of single phase reaction. To confirm the phase behavior, CV measurements of $Na_2FeP_2O_7$ and $Na_2MnP_2O_7$ are also compared (Figure 5b, 5c). This comparison indicates that intercalation/de-intercalation of sodium into/from $Na_2Fe_{0.5}Mn_{0.5}P_2O_7$ takes place through a single phase reaction rather than a biphasic reaction.

In $Na_2MnP_2O_7$ and $Na_2FeP_2O_7$, a two-phase transition is known to occur at ~3.8V and ~3V, respectively [8, 11]. This two-phase reaction region has changed into a single-phase reaction region in $Na_2Fe_{0.5}Mn_{0.5}P_2O_7$ due to the modified Na coordination. However, unlike the upshift of $Fe^{2+/3+}$ redox potential in $Li_2Fe_{1-y}Mn_yP_2O_7$ [23, 24], the redox potential tune ability is not observed in $Na_2Fe_{0.5}Mn_{0.5}P_2O_7$. The existence of single phase reaction during the intercalation/de-intercalation of sodium into/from the host structure was further confirmed by ex-situ XRD analysis (Figure 6). For more clarity the same ex-situ analysis is also presented in small "2θ" range (Figure 6b).

The ex-situ XRD data shows small shifts in "2θ" values for all the crystal planes and confirms the absence of any new phase during extraction/insertion of sodium from the host structure.

This can also be clearly visualized in ex-situ XRD data shown in Figure 6b. During the charging process, the extraction of sodium from the host structure (desodiation), peaks are slightly shifted to higher 2θ values depicting decrease in the lattice parameters due to contraction of the lattice planes. However, during discharging process (sodiation), the peaks are shifted towards small 2θ values undergoing lattice expansion without the formation of any new phase(s). These findings confirm the reversible nature of extraction/insertion of sodium into/from the host structure. The ex-situ analysis thus confirms that the extraction/insertion of sodium in $Na_2Fe_{0.5}Mn_{0.5}P_2O_7$ takes place through a single phase reaction rather than a biphasic reaction. Hence, it can be concluded that a difference in the Na occupancy has a significant role on the structural transformation during charging/discharging and influences the mode of intercalation/de-intercalation of sodium into/from the host structure.

Thermal Stability

Thermogravimetric analyses (TGA) were conducted for $Na_2Fe_{0.5}Mn_{0.5}P_2O_7$ and $Na_2MnP_2O_7$ (Figure 7) to study the thermal stability of the synthesized materials. Upon heating up to 550 °C, TGA data indicates that both as-prepared $Na_2Fe_{0.5}Mn_{0.5}P_2O_7$ and $Na_2MnP_2O_7$ show negligible weight loss (~2%). These thermal stability results are comparable to that of as-prepared $Na_2FeP_2O_7$ [8]. In partially desodiated state (Fig. 7a and 7c), exo/endothermic peaks are barely observable from

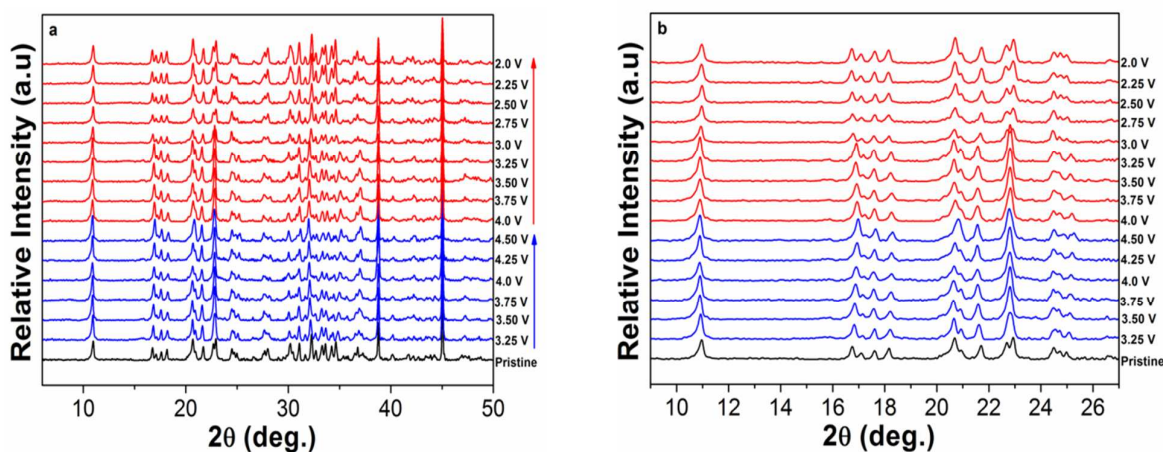**Fig. 6** (a) Ex-situ XRD pattern during charging/discharging for $Na_2Fe_{0.5}Mn_{0.5}P_2O_7$ (b) Ex-situ XRD pattern during charging/discharging for $NaFe_{0.5}Mn_{0.5}P_2O_7$

PCCP

ARTICLE
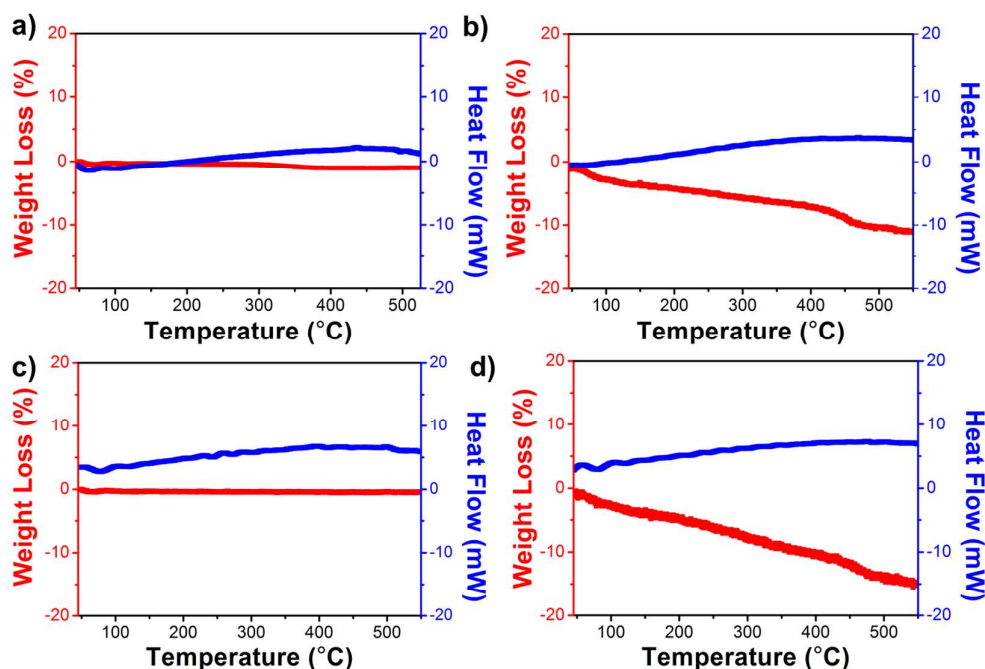
Figure 7. TGA/DTA of: a) $Na_2Fe_{0.5}Mn_{0.5}P_2O_7$ b) desodiated $NaFe_{0.5}Mn_{0.5}P_2O_7$ c) $Na_2MnP_2O_7$ d) desodiated $NaMnP_2O_7$.

differential thermal analysis (DTA) results indicating absence of any phase transformation in both the materials. However, it is evident that the weight loss of partially desodiated $Na_2MnP_2O_7$ is higher than partially desodiated $NaFe_{0.5}Mn_{0.5}P_2O_7$ (Figure 7b and 7d). In fact, the thermal stability of the charged polyanionic materials is affected by transition metals. In general, the high redox potential materials have poor thermal stability [13, 29]. By considering the Li-based counterparts ($LiFeP_2O_7$ and $LiMnP_2O_7$), weight loss of charged (delithiated) electrode of Fe-based polyanionic materials tends to be less than Mn-based polyanionic materials in the same temperature range (e.g. $LiFeP_2O_7$ (~5%) > $Li_{1.4}MnP_2O_7$ (~10%) [13, 30]. Thus, it is important to note that the thermal stability of the desodiated $Na_2MnP_2O_7$ is improved by mixing with Fe.

Conclusions

The solid-solution phase $Na_2Fe_{1-x}Mn_xP_2O_7$(x=0, 0.5, 1) materials

have been synthesized through a solid-state reaction. The synthesized materials adopt a triclinic crystal structure with P-1 space group. The novel mixed pyrophosphate material ($Na_2Fe_{0.5}Mn_{0.5}P_2O_7$) demonstrates a single phase reaction rather than a bi phasic reaction during intercalation/de-intercalation of sodium into/from the host structure. The origin of this single phase behavior can be attributed to different Na coordination environment and different Na sites occupancy in the crystal structure. Both $Fe^{+2/+3}$ and $Mn^{+2/+3}$ redox couples are electrochemically active in $Na_2Fe_{0.5}Mn_{0.5}P_2O_7$ in contrast to its counterpart $Li_2Fe_{0.5}Mn_{0.5}P_2O_7$. The activation of $Mn^{+2/+3}$ redox couple in $Na_2Fe_{0.5}Mn_{0.5}P_2O_7$ can be presumably regarded as the effect of corner-shared Mn sites in the crystal structure that enables it to accommodate Jahn-teller distortion. $Na_2Fe_{0.5}Mn_{0.5}P_2O_7$ demonstrates decent discharge capacity (80mAh/g at C/20) in the voltage range of 2.0 to 4.5 V with average redox potential approximately 3.2V (vs. Na/Na$^+$), good cyclibity (84% capacity retention over 90 cycles) and promising rate capability (70%

capacity retention from 0.05 C to 0.5C). Finally, it can also be concluded that $NaFe_{0.5}Mn_{0.5}P_2O_7$ exhibits good thermal stability both in sodiated (~2% weight loss) and partially desodiated states (~10% weight loss) in the temperature range of 25-550 ℃. In addition, thermal stability of partially desodiated $NaFe_{0.5}Mn_{0.5}P_2O_7$ is found superior to partially desodiated $NaMnP_2O_7$ (~15% weight loss). Therefore, mixed iron–manganese sodium based pyrophosphate cathodes can be attractive for SIBs.

Experimental

Materials and methods

The stoichiometric amounts of precursors, Na_2CO_3 (Aldrich), $(NH_4)_2HPO_4$ (Aldrich), $MnC_2O_4.2H_2O$ (Aldrich) and $FeC_2O_4.2H_2O$ (Aldrich), were thoroughly mixed to synthesize $Na_2Fe_{1-x}Mn_xP_2O_7$ (x=0, 0.5, 1) through a solid-state reaction. The mixed powder was pelletized and calcined under argon atmosphere at 350 °C for 3 hours. After calcination, pellets were cooled to room temperature (in Argon) and were ground into fine powder. This powder was re-pelletized and sintered at 600 °C for 6 hours under argon atmosphere to attain the desired phase. The pellets were cooled to room temperature under argon environment. The powder of the synthesized phase was obtained after grinding. In order to improve the electrical conductivity, the powder was coated with carbon by a high energy ball-milling (500 rpm, 24 h, silicon carbide balls) to yield an 8:2 ratio (wt %) of active material (carbon coating + super P) to carbon. After ball milling, the carbon coated powder was pelletized and annealed at 600 °C for 10 hours under argon atmosphere to restore the crystallinity of the material.

Material Characterization

Powder X-Ray Diffraction (PXRD) measurements of the synthesized material were conducted using a D/MAX-2500 XRD machine (Rigaku, Japan) to analyze phase purity and crystal structure. Thermo-gravimetric analysis and Differential thermal analysis (TGA/DTA) were carried out at a heating rate of 5 °C min^{-1} in Ar atmosphere. Field emission scanning electron microscopy (FE-SEM) was used to study the size and morphology of the pristine material and carbon coated material by using XL30 FEG (Philips, The Netherlands).

Electrochemical Characterization

The carbon-coated (C-coated) active material (75 wt%), carbon black (15 wt%), and polyvinylidene fluoride (PVDF) (10 wt%) were mixed in N-methyl-2-pyrrolidone (NMP) to prepare slurry. The slurry was stirred at 25 °C overnight, and then was casted onto the aluminum foil using the doctor blade technique. The cast samples were dried in an oven at 110 °C for 2 h under vacuum. The samples were then punched at a designated size to assemble coin type half cells (CR2032). The coin cells were prepared in an argon filled glove box by using Na metal disks, 1M sodium perchlorate ($NaClO_4$) in propylene carbonate (PC), and polyethylene separators (Celgard 2400) as

the counter electrode, electrolyte, and separator, respectively. The partially desodiated samples ($NaFe_{0.5}Mn_{0.5}P_2O_7$) for thermal analysis were prepared by charging at 4.5 V and held for 2h. After charging, the cells were disassembled inside a glove box and washed with PC solvent. The cleaned samples were then dried at room temperature. Most of electrochemical testing was performed based on the galvanostatic technique using a battery cycler (WonA Tech, WBCS 3000, Korea) in the potential range of 2.0~4.5 V (vs. Na/Na^+) at room temperature.

Acknowledgements

References

1 M. Armand, J.M. Tarascon, *Nature,* 2008, **451**, 652.
2 D. Kundu, E. Talaie, V. Duffort, L.F. Nazar, *Angew Chem Int Ed.*, 2015, **54**, 3431.
3 V. Palomares, P. Serras, I. Villaluenga, K.B. Hueso, J. Carretero-Gonzalez, T. Rojo, *Energ Environ Sci*, 2012, **5**, 5884.
4 S.W. Kim, D.H. Seo, X.H. Ma, G. Ceder, K. Kang, *Adv Energy Mater*, 2012, **2**, 710.
5 M.D. Slater, D. Kim, E. Lee, C.S. Johnson, *Adv Funct Mater*, 2013, **23**, 947.
6 X.H. Ma, H.L. Chen, G. Ceder, *J Electrochem Soc*, 2011, **158**, A1307.
7 Y.H. Lu, L. Wang, J.G. Cheng, J.B. Goodenough, *Chem Commun*, 2012, **48**, 6544.
8 H. Kim, R.A. Shakoor, C. Park, S.Y. Lim, J.S. Kim, Y.N. Jo, W. Cho, K. Miyasaka, R. Kahraman, Y. Jung, J.W. Choi, *Adv Funct Mater*, 2013, **23**, 1147.
9 P. Barpanda, J.C. Lu, T. Ye, M. Kajiyama, S.C. Chung, N. Yabuuchi, S. Komaba, A. Yamada, *RSC Adv* ,2013, **3**, 3857.
10 P. Barpanda, T. Ye, M. Avdeev, S.C. Chung, A. Yamada, *J Mater Chem A*, 2013, **1**, 4194.
11 C.S. Park, H. Kim, R.A. Shakoor, E. Yang, S.Y. Lim, R. Kahraman, Y. Jung, J.W. Choi, *J Am Chem Soc*, 2013, **135**, 2787.
12 P. Barpanda, T. Ye, S. Nishimura, S.C. Chung, Y. Yamada, M. Okubo, H.S. Zhou, A. Yamada, *Electrochem Commun*, 2012, **24**, 116.
13 M. Tamaru, S.C. Chung, D. Shimizu, S. Nishimura, A. Yamada, *Chem Mater,* 2013, **25**, 2538.
14 S.P. Ong, A. Jain, G. Hautier, B. Kang, G. Ceder, *Electrochem Commun*, 2010, **12**, 427.
15 M.M. Ren, Z. Zhou, Y.Z. Li, X.P. Gao, J. Yan, *J Power Sources*, 2006, **162**, 1357.
16 H.S. Liu, J. Li, Z.R. Zhang, Z.L. Gong, Y. Yang, *Electrochim Acta*, 2004, **49**, 1151.
17 F. Erragh, A. Boukhari, B. Elouadi, E.M. Holt, *J Cryst Spectrosc*, 1991, **21**, 321.
18 Y.F. Shepelev, M.A. Petrova, A.S. Novikova, A.E. Lapshin, *Glass Phys Chem+*, 2002, **28**, 317.
19 F. Erragh, A. Boukhari, F. Abraham, B. Elouadi, *J Solid State Chem*, 1995, **120**, 23.
20 F. Erragh, A. Boukhari, F. Abraham, B. Elouadi, *J Solid State Chem*, 2000, **152**, 323.
21 P. Barpanda, G.D. Liu, C.D. Ling, M. Tamaru, M. Avdeev, S.C. Chung, Y. Yamada, A. Yamada, *Chem Mater*, 2013, **25**, 3480.

22 P. Barpanda, G.D. Liu, Z. Mohamed, C.D. Ling, A. Yamada, *Solid State Ionics*, 2014, **268**, 305.

23 T. Ye, P. Barpanda, S. Nishimura, N. Furuta, S.C. Chung, A. Yamada, *Chem Mater*, 2013, **25**, 3623.

24 H. Zhou, S. Upreti, N.A. Chernova, G. Hautier, G. Ceder, M.S. Whittingham, *Chem Mater*, 2011, **23**, 293.

25 M. Tamaru, P. Barpanda, Y. Yamada, S. Nishimura, A. Yamada, *J Mater Chem*, 2012, **22**, 24526.

26 R. Berthelot, D. Carlier, C. Delmas, *Nat Mater*, 2011, **10**, 74.

27 S. Komaba, N. Yabuuchi, T. Nakayama, A. Ogata, T. Ishikawa, I. Nakai, *Inorg Chem*, 2012, **51**, 6211.

28 D. Carlier, J.H. Cheng, R. Berthelot, M. Guignard, M. Yoncheva, R. Stoyanova, B.J. Hwang, C. Delmas, *Dalton T,* 2011, **52**, 9306.

29 G. Hautier, A. Jain, S.P. Ong, B. Kang, C. Moore, R. Doe, G. Ceder, *Chem Mater*, 2011, **23**, 3495.

30 H. Kim, S. Lee, Y.U. Park, H. Kim, J. Kim, S. Jeon, K. Kang, *Chem Mater*, 2011, **23**, 3930.